Crystal structure of SARS-CoV-2 nsp10 bound to nsp14-ExoN domain reveals an exoribonuclease with both structural and functional integrity

Sheng Lin[1],[†], Hua Chen[1],[†], Zimin Chen[1], Fanli Yang[1], Fei Ye[1], Yue Zheng[1], Jing Yang[1], Xi Lin[1], Honglu Sun[1], Lingling Wang[1], Ao Wen[1], Haohao Dong[2], Qingjie Xiao[3],[4], Dong Deng[3], Yu Cao[1],[5] and Guangwen Lu [1],[6],*

[1]West China Hospital Emergency Department (WCHED), State Key Laboratory of Biotherapy and Cancer Center, West China Hospital and Collaborative Innovation Center of Biotherapy, Sichuan University, Chengdu, Sichuan 610041, China, [2]Laboratory of Aging Research and Cancer Drug Target, State Key Laboratory of Biotherapy and Cancer Center, National Clinical Research Center for Geriatrics, West China Hospital, Sichuan University, Chengdu, Sichuan 610041, China, [3]Department of Obstetrics, Key Laboratory of Birth Defects and Related Disease of Women and Children of MOE, State Key Laboratory of Biotherapy, West China Second Hospital, Sichuan University, Chengdu, Sichuan 610041, China, [4]National Facility for Protein Science in Shanghai, Shanghai Advanced Research Institute (Zhangjiang Laboratory), Chinese Academy of Sciences, Shanghai 201210, China, [5]Disaster Medicine Center, West China Hospital, Sichuan University, Chengdu, Sichuan 610041, China and [6]WestVac Biopharma Co., Ltd, Chengdu, Sichuan 610000, China

ABSTRACT

The emergence of SARS-CoV-2 infection has posed unprecedented threat to global public health. The virus-encoded non-structural protein 14 (nsp14) is a bi-functional enzyme consisting of an exoribonuclease (ExoN) domain and a methyltransferase (MTase) domain and plays a pivotal role in viral replication. Here, we report the structure of SARS-CoV-2 nsp14-ExoN domain bound to its co-factor nsp10 and show that, compared to the SARS-CoV nsp10/nsp14-full-length complex, SARS-CoV-2 nsp14-ExoN retains an integral exoribonuclease fold and preserves an active configuration in the catalytic center. Analysis of the nsp10/nsp14-ExoN interface reveals a foot-print in nsp10 extensively overlapping with that observed in the nsp10/nsp16 structure. A marked difference in the co-factor when engaging nsp14 and nsp16 lies in helix-$\alpha 1'$, which is further experimentally ascertained to be involved in nsp14-binding but not in nsp16-engagement. Finally, we also show that nsp10/nsp14-ExoN is enzymatically active despite the absence of nsp14-MTase domain. These data demonstrate that SARS-CoV-2 nsp10/nsp14-ExoN functions as an exoribonuclease with both structural and functional integrity.

INTRODUCTION

Severe acute respiratory syndrome coronavirus 2 (SARS-CoV-2) is an infectious agent that is currently causing the ongoing pandemic of coronavirus disease 2019 (COVID-19) worldwide (1–3). The virus has led to over 131 million confirmed cases with more than 2.8 million fatalities and spread to 223 countries, areas or territories since first discovered in December 2019 (https://www.who.int/emergencies/diseases/novel-coronavirus-2019, accessed 7 April 2021). While facing the major global public health crisis associated with SARS-CoV-2 transmission and infection (4), it is an urgent issue to develop prophylactic vaccines and anti-viral drugs. Although several vaccines have now been clinically approved, effective drugs remain unavailable despite that significant efforts have been made to combat the virus.

With the same taxonomic hierarchy as severe acute respiratory syndrome coronavirus (SARS-CoV) and Middle East respiratory syndrome coronavirus (MERS-CoV), SARS-CoV-2 belongs to the *Betacoronavirus* genus in the *Coronaviridae* family (5,6). The virus contains a large single-stranded positive-sense RNA genome (∼30 kb). The 5′-terminal two-thirds of the viral genome comprises two overlapping open reading frames (ORF1a and ORF1b), which are initially translated as two large polyproteins (pp1a and pp1ab) followed by proteolytic cleavage into 16 non-structural proteins (nsp1 to nsp16). And the 3′-end of genome encodes four essential structural proteins (spike [S],

*To whom correspondence should be addressed. Tel: +86 28 85502796; Email: lugw@scu.edu.cn
†The authors wish it to be known that, in their opinion, the first two authors should be regarded as Joint First Authors.

envelope [E], membrane [M] and nucleocapsid [N]) and several accessory proteins (7–9). During viral replication, the non-structural proteins assemble into a large membrane bound, multi-subunit transcription/replication machinery (9–11). Within the SARS-CoV-2 replicase machinery, nsp14 is a bifunctional protein with a putative N-terminal exoribonuclease (ExoN) domain playing a proofreading role in RNA replication and an assumed C-terminal guanine-N7-methyltransferase (N7-MTase) domain responsible for mRNA capping (12–14).

Several studies have revealed that coronavirus nsp10 serves as a stimulatory factor for nsp14-ExoN to increase its exoribonuclease activity (13,15). Disruption of the interaction between nsp10 and nsp14 or inactivation of nsp14 exoribonuclease activity would decrease replication fidelity and accelerate the generation of lethal mutagenesis (16–18). Nsp14-ExoN is also implicated in other process of viral life cycle, including the modulation of viral genome recombination (19) and the interference with host innate immune responses (20,21). In addition, the presence of nsp14-ExoN might confer coronavirus specific resistance to nucleoside analogue (NA) drugs (14,18,22,23), which poses great challenge to the development of nsp12 (RNA-dependent RNA polymerase)-targeted nucleoside inhibitors. Therefore, revealing the structural and functional characteristics of SARS-CoV-2 nsp10/nsp14-ExoN heterodimer will not only help understand the mechanism of SARS-CoV-2 RNA proofreading, but also facilitate the development of antiviral inhibitors that could be used alone or in combination with nucleoside analogue (NA) drugs by targeting nsp10/nsp14-ExoN complex.

In this study, we determined the first crystal structure of SARS-CoV-2 nsp10/nsp14-ExoN complex which revealed an exoribonuclease with structural integrity. In addition, our exoribonuclease activity assay further confirmed that the nsp10/nsp14-ExoN complex is functionally active despite the absence of nsp14-N7-MTase domain.

MATERIALS AND METHODS

Cloning, expression and purification

The coding sequences of full-length nsp10 and nsp14 from SARS-CoV-2 (GenBank: MN908947.3) were synthesized (Convenience Biology Corporation) and sub-cloned into pGEX-6p-1 and pET-30a-MBP (modified pET-30a vector that contains an N-terminal MBP tag), respectively. The coding sequences of nsp10-$\Delta\alpha1'$ (residues 22–139), nsp14-ExoN (residues 1–289), nsp14 and nsp14-ExoN active-site mutants (E191A/H268A/D273A) were generated with a standard PCR-based strategy. For recombinant protein production, the plasmids of nsp10 (with an N-terminal GST tag) and nsp14 or nsp14-ExoN (wild-type or active-site mutant, with an N-terminal MBP tag) were co-transformed into *Escherichia coli* BL21 (DE3). The cells containing both plasmids were then grown in LB medium supplemented with 50 μg/ml ampicillin and 25 μg/ml kanamycin at 37°C and induced for protein production with 400 μM isopropyl-β-D-thiogalactopyranoside (IPTG) at 16°C for about 18 h. Cells were harvested, lysed by sonication in re-suspension buffer composed of 10 mM HEPES (pH 7.5) and 250 mM NaCl, and clarified via centrifugation at 18 000 × g for

30 min. Cleared lysate-supernatant was passed over gravity column loaded with Dextrin-Sepharose resin (GE Healthcare), washed with re-suspension buffer, and then eluted with elution buffer containing 10 mM HEPES (pH 7.0), 40 mM NaCl and 20 mM maltose. The two co-expressed fusion proteins were subsequently cleaved by PreScission Protease with the protein-to-enzyme weight-ratio (w/w) of 200:1 in elution buffer supplemented with 1 mM DTT at 4°C for about 6 h. To eliminate the GST and MBP tags, the protein mixture was then loaded onto a cation-exchange column (SOURCE 15S, GE Healthcare) equilibrated with a buffer consisting of 10 mM HEPES (pH 7.0) and 30 mM NaCl, and eluted with an increasing concentration of NaCl. The target proteins were then collected and further purified by gel filtration chromatography in re-suspension buffer using the Superdex 200 Increase 10/300 GL column (GE Healthcare).

Crystallization

Commercial crystallization kits (Molecular Dimensions and Hampton Research) were used for initial crystallization screenings by the vapour-diffusion sitting-drop method. In brief, 1 μl nsp10/nsp14 or nsp10/nsp14-ExoN complex was mixed with 1 μl reservoir solution, and the resultant mixture was then equilibrated against 70 μl reservoir solution at 18°C. Diffractable crystals of the nsp10/nsp14-ExoN complex were obtained in a condition consisting of 0.1 M MOPS (pH 7.5), 0.1 M Magnesium acetate tetrahydrate and 12% w/v PEG 8000 with a protein concentration of 8 mg/ml.

Data collection and structure determination

For data collection, crystals were flash-cooled in liquid nitrogen after a brief soaking in reservoir solution supplemented with 20% (v/v) glycerol. Diffraction data were collected at Shanghai Synchrotron Radiation Facility (SSRF) beamline BL18U1 (24). The collected data were then processed with HKL2000 (25) for indexing, integration and scaling. The structure was solved by molecular replacement with the Phaser program (26) from the CCP4 suite (27), using the structure of SARS-CoV nsp10/nsp14 (PDB code: 5C8T) (13) as the search model. Initial restrained rigid-body refinement was performed using Refmac5 (28), which was followed by manual rebuilding and adjustment in Coot (29), and water molecules were automatically added in Phenix.refine (30). The stereochemical quality of the final model was assessed through the program Procheck (31). Final statistics for data collection and structure refinement are summarized in Supplementary Table S1. All structural figures were generated using PyMOL (https://pymol.org/).

Exoribonuclease activity assay

The exoribonuclease activity assays were carried out in 8 μl reaction system consisting of 20 mM HEPES (pH 7.5), 100 mM NaCl, 5 mM MgCl₂, 1 mM DTT, 6 μM 34-nt unlabelled RNA substrate (5′-CACUAAUAAUAUCAAUGG AUUGAUAUUAUUAAUG-3′, chemically synthesized by Sangon Biotech) and 2-fold serially diluted nsp10/nsp14

(wild type and active-site mutant) or nsp10/nsp14-ExoN (wild type and active-site mutant) ranging from 10 to 1.25 μM. To determine the effect of different divalent metal ions on exoribonuclease activity, the protein concentration was adjusted to 5 μM. Different divalent metal ions, including $MgCl_2$ (10–1.25 mM), $MnCl_2$ (10–1.25 mM), $CaCl_2$ (10–1.25 mM) and $ZnCl_2$ (1–0.125 mM), or 5 mM EDTA were added. After incubation at 37°C for 45 min, the reactions were stopped by the addition of an equal volume of loading buffer (95% formamide, 0.02% SDS, 0.02% bromophenol blue, 0.02% xylene cyanol FF and 10 mM EDTA) and boiled at 95°C for 3 min. The products were then resolved using 7 M urea-containing 18% polyacrylamide gels in 0.5× TBE (Tris–borate–EDTA) buffer. The gel was stained with ethidium bromide (EB, final concentration: 1 μg/ml) for about 10 minutes, and the RNA bands were subsequently visualized with Gel Doc^{TM} XR+ (Bio-Rad).

In order to visualize the cleaved RNA products, we further repeated the exoribonuclease-hydrolysis assay but replaced the unlabelled RNA with the 5′-FAM labelled RNA substrate (5′-FAM-CACUAAUAAUAUCAAUGG AUUGAUAUUAUUAAUG-3′, chemically synthesized by Sangon Biotech). The experiments were performed the same as those with the unlabelled RNA. Instead of staining with EB, however, the RNA bands on gels were directly observed using Gel Doc^{TM} XR+.

GST pull-down assay

Escherichia coli BL21 (DE3) cells were firstly co-transformed with the indicated plasmids in pairs. The cells containing both plasmids were then grown in 50-ml LB medium supplemented with 50 μg/ml ampicillin and 25 μg/ml kanamycin at 37°C and induced for protein production with 400 μM isopropyl-β-D-thiogalactopyranoside (IPTG) at 16°C for about 14 h. Cells were harvested, lysed by sonication in re-suspension buffer consisting of 10 mM HEPES (pH 7.5) and 250 mM NaCl, and clarified via centrifugation at 17 000 × g for 20 min. The resulting supernatants were bound to Glutathione-Sepharose resin (GE Healthcare) for 2 hours and fully washed with washing buffer containing 10 mM HEPES (pH 7.5), 250 mM NaCl and 0.1% (v/v) Tween-20. The resin-bound protein species were then analyzed by SDS-PAGE and visualized by staining with Coomassie blue.

RESULTS

Overall structure of SARS-CoV-2 nsp10/nsp14-ExoN complex

In order to study the structural features of SARS-CoV-2 nsp10/nsp14 exoribonuclease, we initially prepared the hetero-complex protein of full-length nsp14 bound to nsp10 via co-expression of MBP-tagged nsp14 and GST-tagged nsp10 in *E. coli* and subsequent enzymatic cleavage to remove the fused tags (Supplementary Figure S1A and B).

Till this end, however, we were unable to crystallize this full-length nsp10/nsp14 protein complex. Alternatively, we further prepared the hetero-dimeric protein of nsp14-ExoN (amino acids 1–289 of nsp14) in complex with full-length

nsp10 using the same expression and purification strategy as the wild-type proteins. We finally managed to crystallize nsp10/nsp14-ExoN complex and solved the structure at 2.7 Å resolution by molecular replacement. The final model, which was refined to $R_{work} = 0.230$ and $R_{free} = 0.264$, respectively (Supplementary Table S1), contained nsp10 residues A1-D131 and the nsp14-ExoN amino acids N3-K288 with a 1:1 binding mode in the asymmetric unit (Figure 1A and Supplementary Figure S2).

Overall, the nsp10/nsp14-ExoN structure can be seen as an nsp14-ExoN molecule leaning on flank of an nsp10 monomer (Figure 1A). Nsp14-ExoN comprises fifteen β-strands (β1–β15), five α-helices (α1–α5) and six 3_{10} helices (η1–η6) (Supplementary Figures S3A and S4A). Strands β4–β6, β9–β10 and β15 assemble into a centrally located crooked β-sheet and this central sheet is further wrapped by helices α1–α5 and η3–η6 to form a core domain. A peripheral structural entity with a slight convex surface was observed to form by strands β11–β14 and to locate in a close vicinity to the core domain. Extending from the core domain, a second structural entity consisting of strands β1–β3 and β7–β8 and helices η1–η2 protrudes out to make physical contact with nsp10.

As a co-factor for nsp14, nsp10 is composed of three β-strands, four α-helices and two 3_{10} helices, which further assemble into two subdomains (Supplementary Figures S3B and S4B). One subdomain consists of three antiparallel central strands β1′–β3′ and helices η1′–η2′, serving as a basal body. The other subdomain is composed of helices α1′–α4′, sterically locating above the first subdomain.

For amino acid sequence, nsp10 and nsp14-ExoN of SARS-CoV-2 both show high sequence identities with the SARS-CoV homologs (~97% for nsp10 and ~95% for nsp14-ExoN). Accordingly, superimposition of our structure onto the structure of two previously reported SARS-CoV nsp10/nsp14 hetero-complex reveals individually resembled nsp10 and nsp14-ExoN structures, showing a root mean squared deviation (rmsd) of ~0.5 Å/131 Cα pairs (PDB code: 5C8T) [13] and ~0.5 Å/131 Cα pairs (PDB code: 5NFY) [14] for nsp10 and ~0.7 Å/286 Cα pairs (PDB code: 5C8T) and ~0.6 Å/286 Cα pairs (PDB code: 5NFY) for nsp14-ExoN, respectively (Figure 1B). The small differences in the nsp10- and nsp14-primary-sequences between SARS-CoV-2 and SARS-CoV, therefore, had no significant consequences on the protein structure.

It should be noted that within both nsp10 and nsp14-ExoN, two zinc-fingers are observed to form to stabilize the protein structure. For nsp10, two zinc ions are individually coordinated by residues C74/C77/H83/C90 and C117/C120/C128/C130 (Figure 1C). These zinc ions have also been observed in several recently-solved complex structures of SARS-CoV-2 nsp10 bound to nsp16 [32–34]. For nsp14-ExoN, the two zinc-finger motifs are composed of residues C207/C210/C226/H229 and H257/C261/H264/C279, respectively (Figure 1D). The two sites are sterically located near the C-terminal MTase domain (Figure 1B), one bridging the β11/β12 and β13/β14 intervening loops and the other locking the α4/α5 intervening loop to helix α5. It is also notable that these zinc-coordinating residues are individually well-conserved in nsp10 and nsp14 among different beta-coronaviruses, in-
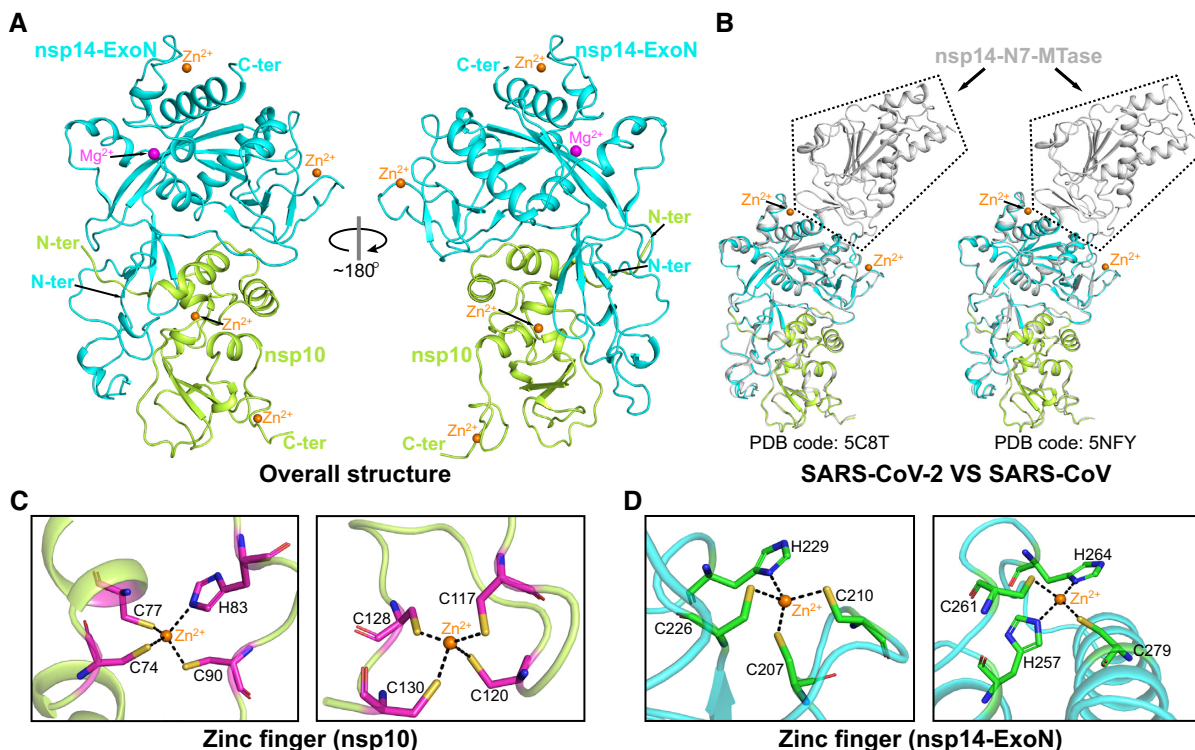
Figure 1. Structure of SARS-CoV-2 nsp10/nsp14-ExoN heterodimer. (**A**) Overall structure of the hetero-complex formed between nsp10 (lemon) and nsp14-ExoN (cyan). Magnesium and zinc ions are shown as spheres and are colored magenta and orange, respectively. (**B**) Superimposition of the SARS-CoV-2 nsp10/nsp14-ExoN structure onto the two previously reported nsp10/nsp14 structure of SARS-CoV (PDB codes: 5C8T and 5NFY) (13,14). The color scheme for our structure is the same as in (A), and the SARS-CoV nsp10/nsp14 structures are shown in gray. The additional nsp14-N7-MTase domains in the SARS-CoV nsp10/nsp14 structures are highlighted and marked. (**C and D**) Magnified views on the two zinc-finger motifs in nsp10 (**C**) and nsp14-ExoN (**D**). Residues involved in zinc-coordination are shown as sticks and zinc ions are shown as spheres.

cluding SARS-CoV-2, SARS-CoV and MERS-CoV (Supplementary Figure S4A and B).

Structural basis of the binding between nsp10 and nsp14-ExoN

To delineate the structural basis of the binding between nsp10 and nsp14-ExoN, we further performed a comprehensive characterization of the atomic interactive details between the two binding entities. Overall, extremely large surface areas ($\sim$2275 Å^2 in nsp10 and $\sim$2136 Å^2 in nsp14-ExoN) are buried upon complex formation. In total, 47 residues from nsp10 and 56 amino acids from nsp14-ExoN were identified to locate along the binding interface (within a distance of 4.5-Å from the binding entity) to provide inter-molecule contacts (Supplementary Table S2). Over half of these amino acids are hydrophilic residues (polar or charged), indicating that the engagement of nsp10 to nsp14-ExoN is predominantly mediated by polar interactions. For nsp10, this co-factor protein utilizes both its subdomains to interact with nsp14 (Figure 2A). The structural elements involved in the binding include helices α1′, α2′, α3′, η1′, strands β2′, β3′ and most of their intervening loops. Reciprocally, nsp14-ExoN mainly uses its two peripheral structural entities (out of the core domain) for nsp10 binding. Along the interface are amino acids from helix η1, strands β2, β8, β11, a long N-terminal loop and multiple intervening loops (β2/β3, β3/α1, β7/β8, α3/β11 and β11/β12).

For clarity, we further divided the interface-elements in nsp10 into four parts and accordingly the extended nsp10/nsp14-ExoN interface into four binding patches (Patch1, 2, 3 and 4) (Figure 2A). The first patch (Patch1) involves a large number of residues in nsp10 helix α1′ and its flanking loops (including A1, N3-P8, T12, S15, F16 and F19-V21) interacting with amino acids in nsp14-ExoN N-terminal loop, helix η1, strand β11 and the β3/α1, α3/β11 and β11/β12 intervening loops (including N3-T5, F8-D10, T25, L27, F60-Y64, Y69, K196, K200 and I201) (Figure 2B). This patch form an extensive interaction network, providing approximately 46% of the total atomic contacts (Supplementary Table S2). In addition, eight hydrogen bonds (nsp10-A1 with nsp14-K9, N3 with D10, E6 with T5, T12 with N63, S15 with K61, F19 with I201, and V21 with I201) are observed to form in this patch, further stabilizing the nsp10/nsp14-ExoN complex. The second patch (Patch2) involves nsp10 helix α2′. On the whole, Patch2 only contributes a limited number of inter-molecule contacts and mainly involves residues D29 and S33 of nsp10 interacting with V66 and Y69 in the β3/α1 intervening loop of nsp14-ExoN (Figure 2C). These amino acids also provide one hydrogen bond, formed between nsp10-D29 and nsp14-Y69. For the third patch (Patch3), five residues (N40 and V42-L45) from the long α2′/β1′ intervening loop of nsp10 and five amino acids (T25-H26, L38-C39 and D41) interspersing over nsp14 N-terminal loop, helix η1, strand β2 and the β2/β3 intervening loop are packed against each other,
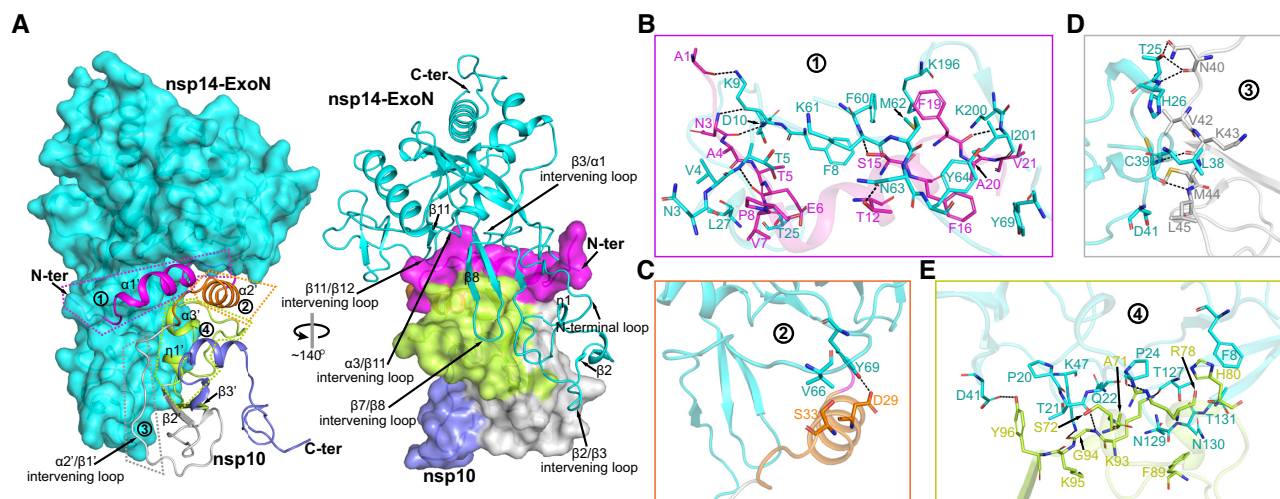
Figure 2. The atomic binding details between SARS-CoV-2 nsp10 and nsp14-ExoN. (**A**) An overview of the binding interface. In the left panel, nsp10 and nsp14-ExoN are shown in cartoon and surface representations, respectively. The interface-elements in nsp10 are labelled and further divided into four parts. The amino acid interaction details related to each part are further illustrated in (**B–E**). In the right panel, nsp10 is shown in surface and nsp14-ExoN in cartoon, and the interface-components in nsp14-ExoN are indicated. (**B**) The interaction of nsp10 helix α1′ and its flanking loops with nsp14-ExoN. (**C**) The interaction of nsp10 helix α2′ with nsp14-ExoN. (**D**) The interaction of nsp10 α2′/β1′ intervening loop with nsp14-ExoN. (**E**) The interaction of nsp10 helices η1′, α3′, strand β3′ and α3′/β3′ intervening loop with nsp14-ExoN. For clarity, only those residues providing ≥10 contacts are shown and labelled. A full list of the interface residues are summarized in Supplementary Table S2. Dashed lines indicate hydrogen-bonds.

providing five hydrogen bonds (nsp10-N40 with nsp14-T25, N40 with H26, K43 with C39, and L45 with C39) and multiple van der Waals (vdw) interactions (Figure 2D). Finally, the fourth patch (Patch4) mainly involves nsp10 helices η1′ and α3′, strand β3′ and α3′/β3′ intervening loop. A series of nsp10 residues (including A71-S72, R78, H80, F89 and K93-Y96) are observed to stack with amino acids in nsp14 N-terminal loop, strand β8, and the β2/β3 and β7/β8 intervening loops (including F8, P20-Q22, P24, D41, K47, T127 and N129-T131), forming an extensive network of vdw and hydrogen-bond (nsp10-R78 with nsp14-P24, K93 with T127, G94 with T21, G94 with K47, and Y96 with D41) interactions (Figure 2E). Taken together, these defined residue contacts, especially the large number of inter-molecule hydrogen bonds, well explain the observed solution stability of the nsp10/nsp14 and nsp10/nsp14-ExoN complexes (Supplementary Figure S1B and E).

## Variant role of nsp10 α1′ helix in nsp14- and nsp16-binding

Inspired by the studies that coronavirus nsp10 functions as a bifunctional protein which could separately bind to and stimulate both nsp16 and nsp14 (10,13,35), we further compared our nsp10/nsp14-ExoN structure with the structures of SARS-CoV-2 nsp10 either in the apo-form or in complex with nsp16 (Figure 3A-D). We found that the majority of the co-factor remained structurally unchanged during complex formation. For example, structural alignment of nsp10 in the nsp14-ExoN-bound state and the apo-state (PDB code: 6ZPE) (36) reveals an rmsd of ∼0.8 Å for 121 Cα pairs. In comparison to nsp10 in the nsp16-bound state, these values are ∼0.7-Å/111-Cα-pairs and ∼1.5-Å/113-Cα-pairs when two recently-reported nsp10/nsp16 structures (PDB codes: 7C2I and 6WVN) (34,37) are used for superimposition. A large conformational difference, however,

was observed for the N-terminal α1′ helix. While the helix retains the same conformation in the apo- and nsp14-ExoN-bound structures, it exhibits quite different conformations in the nsp10/nsp16 structures. In one of the structure (PDB code: 7C2I), this helix is completely density-untraceable; while in the other (PDB code: 6WVN), the helix is visible but is shown to flip by ∼130°, consequently placing α1′ in an almost opposite orientation (Figure 3E–G).

It should be noted that nsp10 helix α1′ is extensively involved in interacting with nsp14 (see Patch1 of the binding interface described in 'Structural basis of the binding between nsp10 and nsp14-ExoN') but is located on the distantly opposite side of the nsp16 binding site. We therefore further conducted pull-down assay to examine the role of the helix in interfacing with different nsp partners. As expected, the full-length nsp10 was readily binding to full-length nsp14, nsp14-ExoN and nsp16. In contrast, nsp10 lacking the N-terminal α1′-helix (nsp10-Δα1′) was observed to only interact with nsp16 but not with either nsp14 or nsp14-ExoN (Supplementary Figure S5). The functional data, therefore, demonstrate that nsp10 α1′ helix plays a key role in binding nsp14 but is dispensable for nsp16-engagement, well echoing our structural observations.

Extensively overlapping nsp14- and nsp16-footprints in nsp10

Facilitated by the structures of nsp10 bound to nsp14-ExoN and nsp16, we further mapped their respective binding sites on the co-factor for comparison. Overall, a markedly more extended surface area in nsp10 is observed to be buried by nsp14-ExoN than by nsp16 (Figure 4A and B). According to the nsp10/nsp16 structure (PDB code: 7C2I), the calculated buried surface area in nsp10 is only ∼933 Å². This value is less than half of that observed for nsp14-
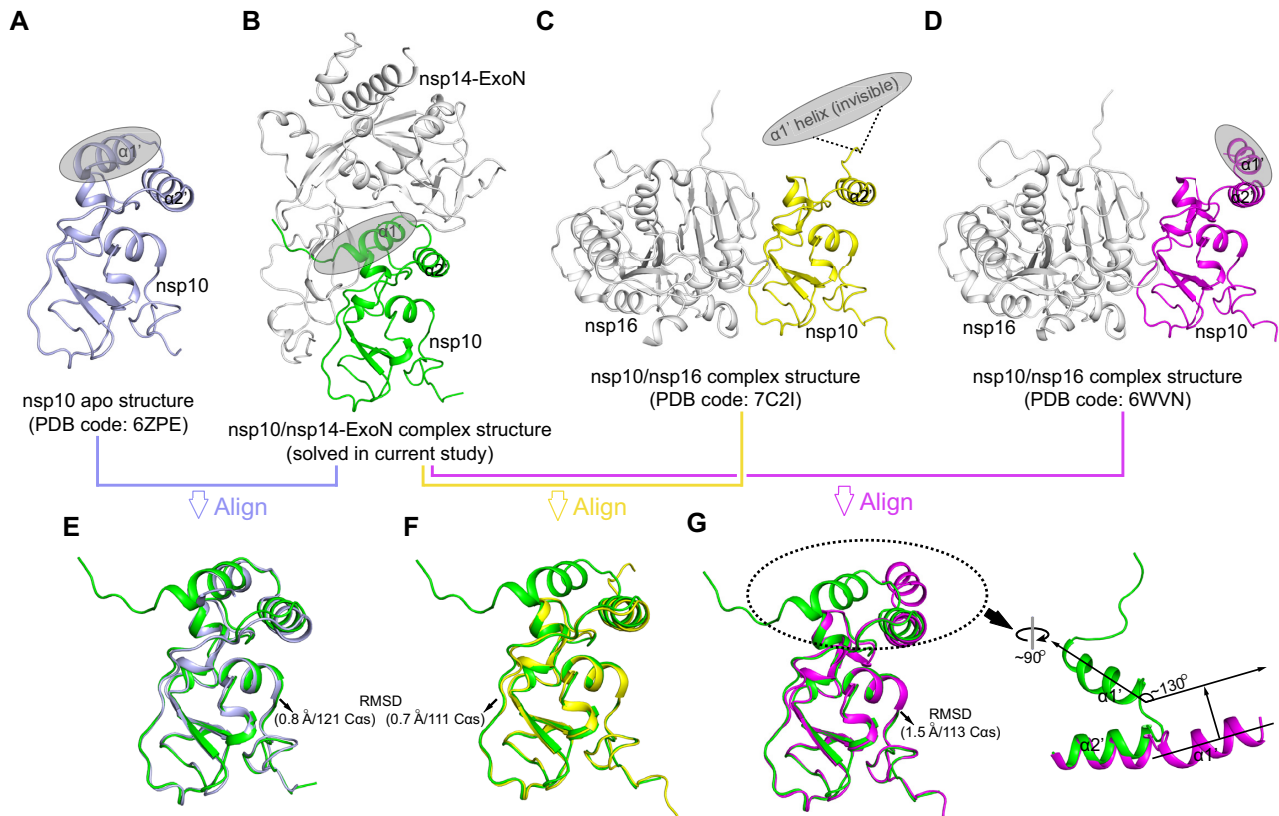
Figure 3. Variant conformations of SARS-CoV-2 nsp10 α1′ helix when engaging nsp14 and nsp16. The structures of nsp10 in the apo-state and in the bound state with nsp14-ExoN or with nsp16 are compared, and a special attention is paid to the nsp10 N-terminal α1′-helix which is highlighted by shaded ellipse. (**A**) The apo structure of SARS-CoV-2 nsp10 (shown in light blue) (PDB code: 6ZPE) (36). (**B**) The structure of SARS-CoV-2 nsp10 (shown in green) bound to nsp14-ExoN (shown in gray) solved in the current study. (**C**) A recently reported complex structure of SARS-CoV-2 nsp10 (shown in yellow) bound to nsp16 (shown in gray) in which nsp10 α1′-helix is invisible (PDB code: 7C2I) (34). (**D**) Another solved complex structure of SARS-CoV-2 nsp10 (shown in magenta) bound to nsp16 (shown in gray) in which nsp10 α1′-helix is visible (PDB code: 6WVN). (**E–G**) Superimposition of the indicated structures. (**E**) Superimposition of the two structures in (A) and (B). (**F**) Superimposition of the two structures in (B) and (C). (**G**) Superimposition of the two structures in (B) and (D). The profound orientation-difference in nsp10 α1′-helix are marked.

ExoN (∼2275 Å²). Further align of the two binding interface shows that the footprints in nsp10 for nsp14-ExoN and nsp16 are extensively overlapping. A large number of nsp10 amino acids, including N40-L45, T58-P59, G69-S72, C77-R78, H80 and K93-Y96 are involved in interacting with both nsp14 and nsp16 (Figure 4C and Supplementary Figure S4B). The two proteins, therefore, should compete with one another for nsp10 binding. It is also notable that the marked difference in nsp10 when engaging nsp14 and nsp16 is largely attributed to the N-terminal α1′ helix in the cofactor (Figure 3B–D). This helix was shown to interact extensively with nsp14-ExoN (Figure 2B) but is devoid of any inter-molecule contacts when engaging nsp16.

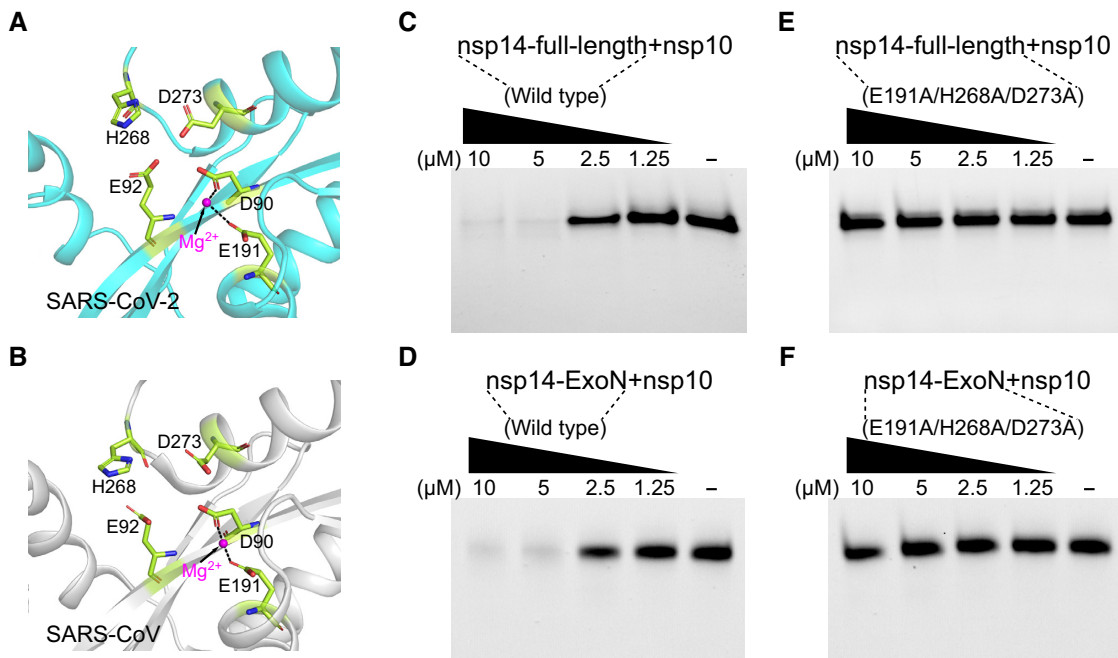## Nsp14 exoribonuclease activity is independent of its C-terminal N7-MTase domain

Coronavirus nsp14-ExoN belongs to the DEDD exonuclease superfamily, which shares a conserved two-metal-ion-assisted mechanism for nucleotide excision (13,38). Previous studies on SARS-CoV nsp14 have revealed that the exoribonuclease catalytic center is composed of five residues (including D90, E92, E191, H268 and D273), which could

coordinate divalent magnesium ions for catalysis (13,39). These five amino acids are absolutely conserved in SARS-CoV-2 nsp14 (Supplementary Figure S4A). We further compared our nsp10/nsp14-ExoN structure with a previously reported SARS-CoV nsp10/nsp14 structure (PDB code: 5C8T) (13) by focusing on the catalytic center. As shown in Figure 5A and B, the five residues in SARS-CoV-2 nsp14-ExoN are sterically clustered together in a way quite similar to that observed in SARS-CoV nsp14. Expectedly, we were also able to trace an Mg²⁺ ion around the catalytic center in our structure, which is coordinated by residues D90 and E191 (Figure 5A). Similar magnesium-coordination pattern has also been observed in the SARS-CoV nsp10/nsp14 structure (Figure 5B).

It is interesting that the configuration of the catalytic center is well preserved in our structure, despite that the C-terminal N7-MTase domain is truncated. We therefore further set up an exoribonuclease-hydrolysis assay in which a 34-nt RNA substrate was digested in the presence of 5 mM MgCl₂ by using different nsp10/nsp14 protein complexes, including nsp10/nsp14, nsp10/nsp14-ExoN, and the active-site mutant proteins nsp10/nsp14-E191A/H268A/D273A and nsp10/nsp14-
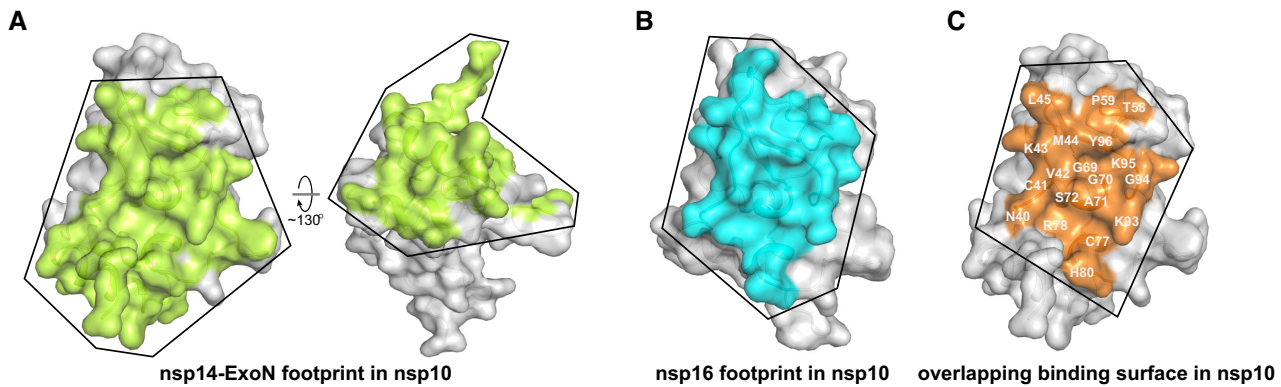
Figure 4. Extensively overlapping nsp14- and nsp16-footprint in nsp10. (**A**) The footprint of nsp14-ExoN in nsp10 (colored by lemon). The extended surface is illustrated in two parts. The first part is overlapped with the nsp16-footprint and is presented on the left side. The second part, which is only buried when engaging nsp14, is presented on the right side. (**B**) The footprint of nsp16 in nsp10 (colored cyan). (**C**) The overlapping surface patch in nsp10 (colored orange). Those residues that are involved in interacting with both nsp14-ExoN and nsp16 are further labelled. The molecule shown on the left side of panel (A) is oriented in the same way as the molecules in panels (B) and (C).

Figure 5. SARS-CoV-2 nsp14 exoribonuclease activity is independent of its C-terminal N7-MTase domain. (A and B) A pairwise comparison of the exoribonuclease active site in nsp14 observed in our structure (**A**) and in a previously reported structure of SARS-CoV nsp10/nsp14 complex (PDB code: 5C8T) (13) (**B**). The catalytic residues are shown as sticks and the magnesium ions observed in the structures are shown as spheres. Dashed lines indicate hydrogen bonds. (C–F) Exoribonuclease-excision assays of 2-fold serially diluted nsp10/nsp14 protein complexes towards a 34-nt unlabelled RNA substrate. (**C**) nsp10/nsp14-full-length protein. (**D**) nsp10/nsp14-ExoN protein. (**E**) nsp10/nsp14-full-length active-site mutant (E191A/H268A/D273A) protein. (**F**) nsp10/nsp14-ExoN active-site mutant (E191A/H268A/D273A) protein.

ExoN-E191A/H268A/D273A. These protein preparations were first purified and their solution behaviors were confirmed by gel filtration chromatography (Supplementary Figure S1B, C, E and F). We first utilized the unlabelled RNA as the substrate and detected the cleavage of the RNA substrate by ethidium bromide (EB) staining. An apparently concentration-dependent RNA hydrolysis, as evidenced by the disappearance of the substrate RNA, was observed with the wild-type nsp10/nsp14 protein. In addition, we recorded a similar concentration-dependent RNA-digestion for nsp10/nsp14-ExoN, demonstrating that this

C-terminally truncated protein form remains exoribonuclease active. As a control, no obvious substrate digestion was observed for the two active-site mutant proteins (Figure 5C–F). In order to view the progressively cleaved products, we further repeated the exoribonuclease-hydrolysis experiments but replaced the unlabelled RNA with a fluorescently (5'-FAM) labelled RNA substrate. As expected, the incompletely digested RNA intermediates, which showed in the gel as a ladder of smaller RNA bands, were clearly traced (Supplementary Figure S6A–D). Taken together, these RNA-hydrolysis data clearly showed that the func-
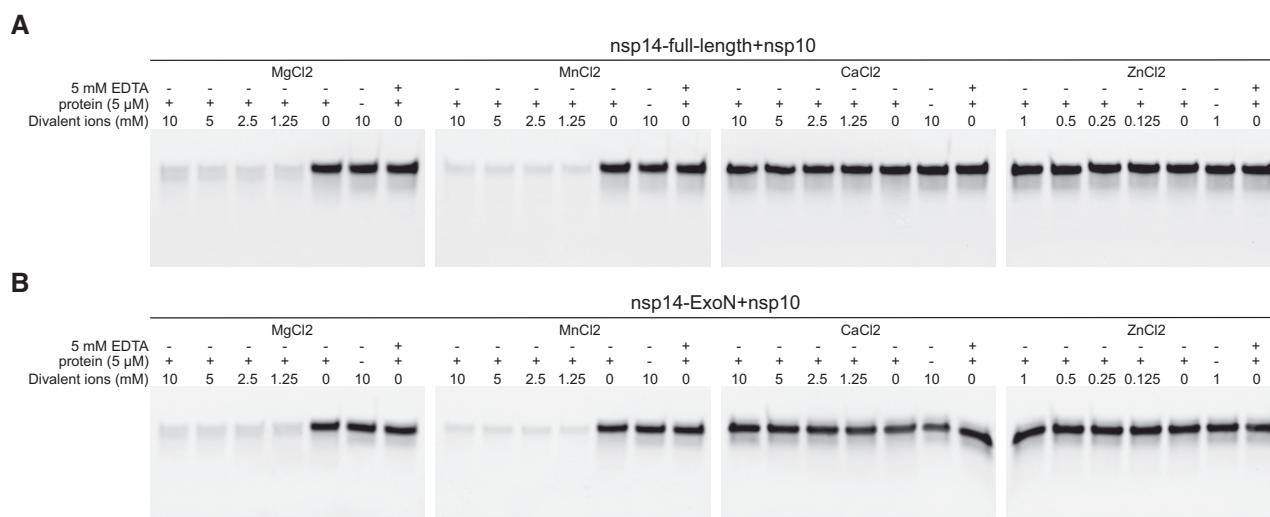
Figure 6. Variant roles of different divalent metal ions on SARS-CoV-2 nsp10/nsp14 exoribonuclease activity. (A and B) The 34-nt unlabelled RNA substrate was hydrolyzed using a fixed concentration (5 μM) of nsp10/nsp14 (**A**) or nsp10/nsp14-ExoN (**B**) in the presence of 2-fold serially diluted divalent metal ions ($MgCl_2$, $MnCl_2$, $CaCl_2$ or $ZnCl_2$) or 5 mM chelating agent (EDTA).

tional capacity of SARS-CoV-2 nsp14 as an exoribonuclease was independent of its C-terminal N7-MTase domain.

Facilitated by the hydrolysis experiments, we further characterized the effects of different divalent metal ions on the exoribonuclease function of SARS-CoV-2 nsp10/nsp14. Common divalent metals, including magnesium, manganese, calcium and zinc, were tested in parallel. As shown in Figure 6A and B, no substrate digestion was observed with either the protein-complex alone (without additional divalent metal ions) or in the presence of EDTA (a chelating agent). Of the four metals tested, magnesium and manganese, but not calcium and zinc, could efficiently activate nsp10/nsp14 and nsp10/nsp14-ExoN towards RNA exonucleolysis. These results demonstrated that the exoribonuclease activity of SARS-CoV-2 nsp10/nsp14 was dependent on divalent ions but showed specific selectivity towards magnesium and manganese. Equivalence of Mg^{2+} and Mn^{2+} is also found in many other enzymatic reactions (40–42).

DISCUSSION

The SARS-CoV-2 global pandemic has posed unprecedented threat to social economy and public health. Therefore, it is urgently needed to reveal the molecular mechanisms underlying SARS-CoV-2 replication to accelerate the development of antiviral drugs. Based on previous experience of working with related coronaviruses, many SARS-CoV-2 virus-encoded non-structural proteins have already been quickly functionally and structurally characterized (32,43–47). Nevertheless, the atomic structure of SARS-CoV-2 nsp14, which was supposed to contain both 3′-5′ exoribonuclease and N7-MTase activities, has not been reported thus far. Here, we focus on the 3′-5′ exoribonuclease domain of SARS-CoV-2 nsp14 and report the crystal structure of nsp14-ExoN in complex with its co-factor nsp10. Comparison of our structure with that of SARS-CoV nsp10/nsp14 complex reveals highly similar overall

protein fold and essentially the same configuration of the catalytic center, indicating a conserved mechanism in RNA hydrolysis between the two viruses. This highlights the possibility of developing broad-spectrum inhibitors by targeting nsp14-ExoN. It should be noted that the intrinsic function of coronavirus nsp14-ExoN to correct mismatches during viral genome synthesis has posed great challenges to screen and/or design the nucleoside analogue (NA) drugs by targeting nsp12 polymerase (14,23,48). The nsp14-ExoN inhibitors would therefore likely exhibit synergistic antiviral activity when used in combination with NA drugs such as Ribavirin and Remdesivir.

Via structural comparison, we further explore the nsp14- and nsp16-footprints in SARS-CoV-2 nsp10, and show that the regions of nsp10 interfacing with nsp14-ExoN and nsp16 are extensively overlapping (Figure 4C). Nsp14 and nsp16 should therefore compete with one another for nsp10 binding. In that case, nsp10/nsp14/nsp16 can not form triple complex. It is noteworthy that the nsp10 coding region is located in ORF1a, the protein production from which is expected to be higher than that from ORF1b within which the nsp14 and nsp16 coding regions situate (9,49,50). Thus, this likely represents a mechanism on how the production of non-structural proteins are coordinated to ensure a balance between nsp10/nsp14 and nsp10/nsp16 complex formation and subsequently the maximization of enzymatic activity for virus replication. Such evolutionary difference in the amount of nsp10, nsp14 and nsp16 is likely important for the viral replicative process, which might be studied in the future. In addition, this overlapping interface in nsp10 might also be targeted for design of two-in-one small-molecule or peptidomimetic inhibitors by simultaneously blocking nsp10 binding to both nsp14 exoribonuclease and nsp16 2′-O-methyltransferase.

It is interesting that, to our knowledge, the structure of nsp10 bound to nsp14-ExoN alone and the functional competency of such complex as an exoribonuclease have never been reported previously in any other coronaviruses.

In the current study, we successfully solve the structure of SARS-CoV-2 nsp10/nsp14-ExoN complex, with which we demonstrate that both the overall protein fold and the key structural elements (including the zinc-binding sites and the catalytic center) are well preserved. We further show that SARS-CoV-2 nsp10/nsp14-ExoN possesses the exoribonuclease activity and is able to hydrolyze the 34-nt RNA substrate as efficiently as the wild-type full-length protein. In addition, our RNA-hydrolysis assay clearly shows a similar exoribonuclease-activation pattern by divalent metal ions between nsp10/nsp14-ExoN and full-length nsp10/nsp14. Taken together, we believe these data represent solid evidence that SARS-CoV-2 nsp10/nsp14-ExoN is of both structural and functional integrity as an exoribonuclease. We also noted that several previous studies focusing on the inter-domain functional relations between exoribonuclease and N7-MTase of SARS-CoV nsp14 have shown that mutations in the MTase domain could affect and in some cases even abolish nsp14's exoribonuclease activity (14,51). We tentatively speculate that this might result from an alteration of the complex-protein behavior in solution (e.g., misfolding, aggregation, etc.) due to the mutations and/or may be the result of subtle differences in the primary sequence between SARS-CoV-2 and SARS-CoV nsp14 proteins.

Previous studies on the SARS-CoV nsp10/nsp14 complex have shown that the enzyme possesses a processive 3′-to-5′ exoribonuclease activity, such that several bands of the limited cleavage products could be visualized (13,15,52,53). In these experiments, the RNA substrates are, without exception, radioactively or fluorescently labelled to increase the detection sensitivity. Consistently, we are able to trace such incompletely digested RNA intermediates using the 5′-FAM labelled RNA as the substrate in our exoribonuclease activity assay. Nevertheless, we only observe the cleavage of the RNA but fail to visualize the progressively cleaved products when an unlabelled RNA is used and the RNA is detected by EB staining. Although it is commonly used for nucleic acid visualization, EB staining is much less sensitive than radioactive detection and is also commonly affected by the length of the nucleic acid chain. While the substrate cleavage by the nsp10/nsp14 enzyme would produce a series of products of smaller size, the relatively small amount of each product and its smaller size should explain their invisibility during EB staining. It should be noted that, in our experiments, we have shown that depletion of the divalent metal ions could abolish the substrate cleavage. In addition, the active-site mutants of nsp10/nsp14 and nsp10/nsp14-ExoN, which are prepared in the same way as the wild-type proteins, expectedly do not cleave the substrate RNA. All these results reveal that the disappearance of the substrate in EB staining is unlikely the degradation of the RNA resulted from contaminations, if any, during the enzyme preparation but the reflection of the cleavage by the exoribonuclease. We therefore believe that, by monitoring the substrate cleavage, our assay has provided an alternative yet more convenient method for *in vitro* evaluation of the nsp10/nsp14 exoribonuclease activity by using the unlabelled RNA substrate.

In conclusion, we have provided the mechanistic insight into how SARS-CoV-2 nsp10/nsp14-ExoN exerts its exoribonuclease activity. The structural and functional data reported in this study should be able to aid in the development of antiviral drugs against SARS-CoV-2, which are urgently needed as the confirmed cases of COVID-19 continue to surge.

DATA AVAILABILITY

Atomic coordinates and structure factors for the reported crystal structure have been deposited with the Protein Data Bank under accession number 7DIY.

SUPPLEMENTARY DATA

Supplementary Data are available at NAR Online.

ACKNOWLEDGEMENTS

FUNDING

REFERENCES

1. Coronaviridae Study Group of the International Committee on Taxonomy of Viruses. (2020) The species severe acute respiratory syndrome-related coronavirus: classifying 2019-nCoV and naming it SARS-CoV-2. *Nat. Microbiol.*, **5**, 536–544.
2. Zhou,P., Yang,X.L., Wang,X.G., Hu,B., Zhang,L., Zhang,W., Si,H.R., Zhu,Y., Li,B., Huang,C.L. *et al.* (2020) A pneumonia outbreak associated with a new coronavirus of probable bat origin. *Nature*, **579**, 270–273.
3. Zhu,N., Zhang,D., Wang,W., Li,X., Yang,B., Song,J., Zhao,X., Huang,B., Shi,W., Lu,R. *et al.* (2020) A novel coronavirus from patients with Pneumonia in China,2019. *N. Engl. J. Med.*, **382**, 727–733.
4. Cobey,S. (2020) Modeling infectious disease dynamics. *Science*, **368**, 713–714.
5. Kim,D., Lee,J.Y., Yang,J.S., Kim,J.W., Kim,V.N. and Chang,H. (2020) The architecture of SARS-CoV-2 transcriptome. *Cell*, **181**, 914–921.
6. Hu,B., Guo,H., Zhou,P. and Shi,Z.L. (2021) Characteristics of SARS-CoV-2 and COVID-19. *Nat. Rev. Microbiol.*, **19**, 141–154.
7. Ye,Z.W., Yuan,S., Yuen,K.S., Fung,S.Y., Chan,C.P. and Jin,D.Y. (2020) Zoonotic origins of human coronaviruses. *Int J Biol Sci*, **16**, 1686–1697.

8. Peng,Y., Du,N., Lei,Y., Dorje,S., Qi,J., Luo,T., Gao,G.F. and Song,H. (2020) Structures of the SARS-CoV-2 nucleocapsid and their perspectives for drug design. *EMBO J.*, **39**, e105938.

9. V'Kovski,P., Kratzel,A., Steiner,S., Stalder,H. and Thiel,V. (2021) Coronavirus biology and replication: implications for SARS-CoV-2. *Nat. Rev. Microbiol.*, **19**, 155–170.

10. Chen,Y., Su,C., Ke,M., Jin,X., Xu,L., Zhang,Z., Wu,A., Sun,Y., Yang,Z., Tien,P. *et al.* (2011) Biochemical and structural insights into the mechanisms of SARS coronavirus RNA ribose 2′-O-methylation by nsp16/nsp10 protein complex. *PLoS Pathog.*, **7**, e1002294.

11. Peng,Q., Peng,R., Yuan,B., Zhao,J., Wang,M., Wang,X., Wang,Q., Sun,Y., Fan,Z., Qi,J. *et al.* (2020) Structural and biochemical characterization of the nsp12-nsp7-nsp8 core polymerase complex from SARS-CoV-2. *Cell Rep.*, **31**, 107774.

12. Chen,Y., Cai,H., Pan,J., Xiang,N., Tien,P., Ahola,T. and Guo,D. (2009) Functional screen reveals SARS coronavirus nonstructural protein nsp14 as a novel cap N7 methyltransferase. *Proc. Natl. Acad. Sci. U.S.A.*, **106**, 3484–3489.

13. Ma,Y., Wu,L., Shaw,N., Gao,Y., Wang,J., Sun,Y., Lou,Z., Yan,L., Zhang,R. and Rao,Z. (2015) Structural basis and functional analysis of the SARS coronavirus nsp14-nsp10 complex. *Proc. Natl. Acad. Sci. US.A.*, **112**, 9436–9441.

14. Ferron,F., Subissi,L., Silveira De Morais,A.T., Le,N.T.T., Sevajol,M., Gluais,L., Decroly,E., Vonrhein,C., Bricogne,G., Canard,B. *et al.* (2018) Structural and molecular basis of mismatch correction and ribavirin excision from coronavirus RNA. *Proc. Natl. Acad. Sci. U.S.A.*, **115**, E162–E171.

15. Bouvet,M., Imbert,I., Subissi,L., Gluais,L., Canard,B. and Decroly,E. (2012) RNA 3′-end mismatch excision by the severe acute respiratory syndrome coronavirus nonstructural protein nsp10/nsp14 exoribonuclease complex. *Proc. Natl. Acad. Sci. U.S.A.*, **109**, 9372–9377.

16. Eckerle,L.D., Becker,M.M., Halpin,R.A., Li,K., Venter,E., Lu,X., Scherbakova,S., Graham,R.L., Baric,R.S., Stockwell,T.B. *et al.* (2010) Infidelity of SARS-CoV Nsp14-exonuclease mutant virus replication is revealed by complete genome sequencing. *PLoS Pathog.*, **6**, e1000896.

17. Smith,E.C., Case,J.B., Blanc,H., Isakov,O., Shomron,N., Vignuzzi,M. and Denison,M.R. (2015) Mutations in coronavirus nonstructural protein 10 decrease virus replication fidelity. *J. Virol.*, **89**, 6418–6426.

18. Smith,E.C., Blanc,H., Surdel,M.C., Vignuzzi,M. and Denison,M.R. (2013) Coronaviruses lacking exoribonuclease activity are susceptible to lethal mutagenesis: evidence for proofreading and potential therapeutics. *PLoS Pathog.*, **9**, e1003565.

19. Gribble,J., Stevens,L.J., Agostini,M.L., Anderson-Daniels,J., Chappell,J.D., Lu,X., Pruijssers,A.J., Routh,A.L. and Denison,M.R. (2021) The coronavirus proofreading exoribonuclease mediates extensive viral recombination. *PLoS Pathog.*, **17**, e1009226.

20. Case,J.B., Li,Y., Elliott,R., Lu,X., Graepel,K.W., Sexton,N.R., Smith,E.C., Weiss,S.R. and Denison,M.R. (2018) Murine hepatitis virus nsp14 exoribonuclease activity is required for resistance to innate immunity. *J. Virol.*, **92**, e01531-17.

21. Becares,M., Pascual-Iglesias,A., Nogales,A., Sola,I., Enjuanes,L. and Zuniga,S. (2016) Mutagenesis of coronavirus nsp14 reveals its potential role in modulation of the innate immune response. *J. Virol.*, **90**, 5399–5414.

22. Agostini,M.L., Andres,E.L., Sims,A.C., Graham,R.L., Sheahan,T.P., Lu,X., Smith,E.C., Case,J.B., Feng,J.Y., Jordan,R. *et al.* (2018) Coronavirus susceptibility to the antiviral Remdesivir (GS-5734) is mediated by the viral polymerase and the proofreading exoribonuclease. *mBio*, **9**, e00221-18.

23. Jockusch,S., Tao,C., Li,X., Chien,M., Kumar,S., Morozova,I., Kalachikov,S., Russo,J.J. and Ju,J. (2020) Sofosbuvir terminated RNA is more resistant to SARS-CoV-2 proofreader than RNA terminated by Remdesivir. *Sci. Rep.*, **10**, 16577.

24. Zhang,W.-Z., Tang,J.-C., Wang,S.-S., Wang,Z.-J., Qin,W.-M. and He,J.-H. (2019) The protein complex crystallography beamline (BL19U1) at the Shanghai Synchrotron Radiation Facility. *Nucl. Sci. Tech.*, **30**, 170.

25. Otwinowski,Z. and Minor,W. (1997) Processing of X-ray diffraction data collected in oscillation mode. *Methods Enzymol.*, **276**, 307–326.

26. Read,R.J. (2001) Pushing the boundaries of molecular replacement with maximum likelihood. *Acta Crystallogr. D. Biol. Crystallogr.*, **57**, 1373–1382.

27. Collaborative Computational Project, N. (1994) The CCP4 suite: programs for protein crystallography. *Acta Crystallogr. D. Biol. Crystallogr.*, **50**, 760–763.

28. Murshudov,G.N., Skubak,P., Lebedev,A.A., Pannu,N.S., Steiner,R.A., Nicholls,R.A., Winn,M.D., Long,F. and Vagin,A.A. (2011) REFMAC5 for the refinement of macromolecular crystal structures. *Acta Crystallogr. D. Biol. Crystallogr.*, **67**, 355–367.

29. Emsley,P. and Cowtan,K. (2004) Coot: model-building tools for molecular graphics. *Acta Crystallogr. D. Biol. Crystallogr.*, **60**, 2126–2132.

30. Adams,P.D., Afonine,P.V., Bunkoczi,G., Chen,V.B., Davis,I.W., Echols,N., Headd,J.J., Hung,L.W., Kapral,G.J., Grosse-Kunstleve,R.W. *et al.* (2010) PHENIX: a comprehensive Python-based system for macromolecular structure solution. *Acta Crystallogr. D. Biol. Crystallogr.*, **66**, 213–221.

31. Laskowski,R.A., Macarthur,M.W., Moss,D.S. and Thornton,J.M.J. (1993) PROCHECK: a program to check the stereochemical quality of protein structures. *J. Appl. Crystallogr.*, **26**, 283–291.

32. Viswanathan,T., Arya,S., Chan,S.H., Qi,S., Dai,N., Misra,A., Park,J.G., Oladunni,F., Kovalskyy,D., Hromas,R.A. *et al.* (2020) Structural basis of RNA cap modification by SARS-CoV-2. *Nat. Commun.*, **11**, 3718.

33. Krafcikova,P., Silhan,J., Nencka,R. and Boura,E. (2020) Structural analysis of the SARS-CoV-2 methyltransferase complex involved in RNA cap creation bound to sinefungin. *Nat. Commun.*, **11**, 3717.

34. Lin,S., Chen,H., Ye,F., Chen,Z., Yang,F., Zheng,Y., Cao,Y., Qiao,J., Yang,S. and Lu,G. (2020) Crystal structure of SARS-CoV-2 nsp10/nsp16 2′-O-methylase and its implication on antiviral drug design. *Signal Transduct. Target Ther.*, **5**, 131.

35. Bouvet,M., Lugari,A., Posthuma,C.C., Zevenhoven,J.C., Bernard,S., Betzi,S., Imbert,I., Canard,B., Guillemot,J.C., Lecine,P. *et al.* (2014) Coronavirus Nsp10, a critical co-factor for activation of multiple replicative enzymes. *J. Biol. Chem.*, **289**, 25783–25796.

36. Rogstam,A., Nyblom,M., Christensen,S., Sele,C., Talibov,V.O., Lindvall,T., Rasmussen,A.A., Andre,I., Fisher,Z., Knecht,W. *et al.* (2020) Crystal structure of non-structural protein 10 from severe acute respiratory syndrome coronavirus-2. *Int. J. Mol. Sci.*, **21**, 7375.

37. Rosas-Lemus,M., Minasov,G., Shuvalova,L., Inniss,N.L., Kiryukhina,O., Brunzelle,J. and Satchell,K.J.F. (2020) High-resolution structures of the SARS-CoV-2 2′-O-methyltransferase reveal strategies for structure-based inhibitor design. *Sci. Signal*, **13**, eabe1202.

38. Chen,P., Jiang,M., Hu,T., Liu,Q., Chen,X.S. and Guo,D. (2007) Biochemical characterization of exoribonuclease encoded by SARS coronavirus. *J. Biochem. Mol. Biol.*, **40**, 649–655.

39. Robson,F., Khan,K.S., Le,T.K., Paris,C., Demirbag,S., Barfuss,P., Rocchi,P. and Ng,W.L. (2020) Coronavirus RNA proofreading: molecular basis and therapeutic targeting. *Mol. Cell*, **79**, 710–727.

40. Ye,R.W., Zielinski,N.A. and Chakrabarty,A.M. (1994) Purification and characterization of phosphomannomutase/phosphoglucomutase from Pseudomonas aeruginosa involved in biosynthesis of both alginate and lipopolysaccharide. *J. Bacteriol.*, **176**, 4851–4857.

41. Komori,K., Sakae,S., Fujikane,R., Morikawa,K., Shinagawa,H. and Ishino,Y. (2000) Biochemical characterization of the hjc holliday junction resolvase of *Pyrococcus furiosus*. *Nucleic. Acids. Res.*, **28**, 4544–4551.

42. Cochran,J.C., Zhao,Y.C., Wilcox,D.E. and Kull,F.J. (2011) A metal switch for controlling the activity of molecular motor proteins. *Nat. Struct. Mol. Biol.*, **19**, 122–127.

43. Thoms,M., Buschauer,R., Ameismeier,M., Koepke,L., Denk,T., Hirschenberger,M., Kratzat,H., Hayn,M., Mackens-Kiani,T., Cheng,J. *et al.* (2020) Structural basis for translational shutdown and immune evasion by the Nsp1 protein of SARS-CoV-2. *Science*, **369**, 1249–1255.

44. Jin,Z., Du,X., Xu,Y., Deng,Y., Liu,M., Zhao,Y., Zhang,B., Li,X., Zhang,L., Peng,C. *et al.* (2020) Structure of M(pro) from SARS-CoV-2 and discovery of its inhibitors. *Nature*, **582**, 289–293.

45. Chen,J., Malone,B., Llewellyn,E., Grasso,M., Shelton,P.M.M., Olinares,P.D.B., Maruthi,K., Eng,E.T., Vatandaslar,H., Chait,B.T. *et al.* (2020) Structural basis for helicase-polymerase coupling in the SARS-CoV-2 replication-transcription complex. *Cell*, **182**, 1560–1573.

46. Kim,Y., Jedrzejczak,R., Maltseva,N.I., Wilamowski,M., Endres,M., Godzik,A., Michalska,K. and Joachimiak,A. (2020) Crystal structure

of Nsp15 endoribonuclease NendoU from SARS-CoV-2. *Protein Sci.*, **29**, 1596–1605.

47. Littler,D.R., Gully,B.S., Colson,R.N. and Rossjohn,J. (2020) Crystal structure of the SARS-CoV-2 non-structural protein 9, Nsp9. *iScience*, **23**, 101258.

48. Shannon,A., Le,N.T., Selisko,B., Eydoux,C., Alvarez,K., Guillemot,J.C., Decroly,E., Peersen,O., Ferron,F. and Canard,B. (2020) Remdesivir and SARS-CoV-2: structural requirements at both nsp12 RdRp and nsp14 Exonuclease active-sites. *Antiviral Res.*, **178**, 104793.

49. Hartenian,E., Nandakumar,D., Lari,A., Ly,M., Tucker,J.M. and Glaunsinger,B.A. (2020) The molecular virology of coronaviruses. *J. Biol. Chem.*, **295**, 12910–12934.

50. Finkel,Y., Mizrahi,O., Nachshon,A., Weingarten-Gabbay,S., Morgenstern,D., Yahalom-Ronen,Y., Tamir,H., Achdout,H.,

Stein,D., Israeli,O. *et al.* (2021) The coding capacity of SARS-CoV-2. *Nature*, **589**, 125–130.

51. Chen,Y., Tao,J., Sun,Y., Wu,A., Su,C., Gao,G., Cai,H., Qiu,S., Wu,Y., Ahola,T. *et al.* (2013) Structure-function analysis of severe acute respiratory syndrome coronavirus RNA cap guanine-N7-methyltransferase. *J. Virol.*, **87**, 6296–6305.

52. Minskaia,E., Hertzig,T., Gorbalenya,A.E., Campanacci,V., Cambillau,C., Canard,B. and Ziebuhr,J. (2006) Discovery of an RNA virus $3' \rightarrow 5'$ exoribonuclease that is critically involved in coronavirus RNA synthesis. *Proc. Natl. Acad. Sci. U.S.A.*, **103**, 5108–5113.

53. Subissi,L., Posthuma,C.C., Collet,A., Zevenhoven-Dobbe,J.C., Gorbalenya,A.E., Decroly,E., Snijder,E.J., Canard,B. and Imbert,I. (2014) One severe acute respiratory syndrome coronavirus protein complex integrates processive RNA polymerase and exonuclease activities. *Proc. Natl. Acad. Sci. U.S.A.*, **111**, E3900–E3909.